

Long-term instability of water in oil microdroplets

Tamas Gerecsei ^{1,2}, Rita Ungai-Salanki ¹, Andras Saftics ², Imre Derenyi ^{1,3}, Robert Horvath ², and Balint Szabo ¹

¹ *Department of Biological Physics, Eotvos Lorand University, Budapest, Hungary*

² *Centre for Energy Research, Institute of Technical Physics and Materials Science, Nanobiosensorics Laboratory, Budapest, Hungary and*

³ *MTA-ELTE Statistical and Biological Physics Research Group, Budapest, Hungary*

Water in oil emulsions have a wide range of applications from chemical technology to microfluidics, where the stability of water droplets is of paramount importance. Here we describe and experimentally characterize a yet overlooked phenomenon, the dissolution of water in oil, which renders nanoliter-sized droplets unstable, resulting in their shrinkage and disappearance in a time scale of hours. The rate of dissolution is determined by the product of the diffusion coefficient and the saturation density of water in oil, which also provides a novel method to measure either of these parameters.

Keywords: emulsion, droplet microfluidics, diffusion, saturation concentration, single-cell

I. INTRODUCTION

Water in oil (w/o) emulsions consist of a continuous oil phase with dispersed water droplets. Such arrangements are common both in industrial and laboratory settings [1, 2]. Notably, the field of droplet microfluidics widely uses w/o emulsions for containing reagents and chemical reactions such as polymerase chain reaction (PCR) or other genetic amplification and sequencing methodologies [3, 4]. The droplet-based approach has several advantages, mainly that the volume of the droplets not only matches the desirable size range for single-cell and single-molecule manipulations, but it also minimizes the amount of reagents needed. Such setups have been successfully commercialized and they proved to be a revolutionary tool in single-cell analysis [5]. These advancements have opened the way for the development of lab-on-a-chip devices [6] that are capable of integrating entire bioassay workflows on handheld microfluidic chips.

Over the years, a wide range of techniques have been developed for the precise generation and manipulation (fusion, splitting, transport, etc.) of droplets in the size range of 1 – 100 μm [1, 7]. Such systems are based on micrometer sized channels in microfluidic devices with different geometries in which the droplets are typically created at the junction of a water and an oil containing channel. Important aspects of droplet generation include throughput, monodispersity and the stability of the analyte concentrations inside the droplet [8]. Once created, the volume of the droplets needs to stay constant for the entire duration of the workflow without merging or breaking up. If the volume were to change during an assay or experiment, the concentration of reagents in the droplet would be altered, thus, one of the fundamental functions of the carrier oil (volume conservation by impeding evaporation) would diminish. Merging is an important issue, since most applications utilize a dense emulsion, which means that the overall volume of the water is superior (or comparable) to that of the carrier oil [9, 10]. In these systems there is a physical contact between the interfaces of the droplets that needs to be stabilized by the addition of surfactants [11].

These amphipathic substances associate on the oil/water interface and prevent the coalescence of droplets.

Any oil used in microfluidics needs to comply with some basic requirements such as chemical inertness, biocompatibility, good optical qualities (transparency) and the existence of compatible surfactants. Over the years, the most popular oils that fulfill the above requirements proved to be mineral, silicone, and fluorinated oils [11]. Since oil and water are immiscible due to the apolar and polar nature of their molecules, one would expect a water droplet surrounded by oil to retain its volume for an extended period of time. Even in certain sparse w/o emulsion-based applications the droplets have been reported to be stable for several hours [12].

Without any protective oil layer, droplets rapidly evaporate into the atmosphere. This process has been investigated in depth both theoretically [13] and experimentally [14]. In early studies, mainly the evaporation rate was considered, meaning the amount of volume lost over time [15]. Later however, other shape descriptors were also investigated [16]. In general, two modes of evaporation from a solid surface have been identified: in the so-called 'pinning' mode the contact area of the droplet formed with the solid surface is constant while the contact angle decreases, whereas in the 'shrinking' mode, the contact area shrinks, while the contact angle remains unchanged. Wetting hysteresis, which is the variability of the contact angle between two extremes (the receding and advancing angles) plays an important role in switching between the two modes. A mixed mode where both quantities are simultaneously diminishing has also been described and experimentally observed [17]. While the research done on the topic is extensive and illuminating, it has been focusing on drops exposed to air under standard atmospheric conditions. Mass transfer of a liquid droplet into another miscible liquid has been modeled theoretically by Epstein and Plesset [18] inspiring several experimental studies [19, 20]. Schmitt et al. considered the mass transfer of water droplets in an immiscible oil environment with added emulsifier (Span80) [21]. They found

that the droplet surface exhibited spontaneous microstructure formation decreasing the volume and distorting the shape of the initially spherical droplets.

In the present paper we investigate the long-term stability of thousands of water droplets in sparse w/o emulsions. Emulsions in various oils were generated using a rotating fluid-based method. Subsequently, the droplets were imaged using time-lapse microscopy and a modified contact angle measurement setup to investigate the time evolution of their shape descriptors. We found that microscopic water droplets dissolve into the surrounding oil and that this phenomenon can be described reasonably well with a model similar to evaporation from a surface in atmospheric conditions. After theoretical considerations, we were able to show that the quantity characterizing droplet instability is the product of the diffusion coefficient and the saturation density of water in oil. Our experiments explicitly show, for the first time, that cover oils do not impede the dissolution of microscopic water droplets in sparse emulsions.

II. MATERIALS AND METHODS

A. Droplet generation

Water in oil emulsions were generated using a rotating fluid-based method (similar to [22]) illustrated in Fig. S1. A standard plastic, hydrophobic Petri dish (Greiner) with a diameter of 35 mm was placed onto a rotating platform, then filled with 1 ml oil using a handheld pipette. The following oils were investigated: mineral oil, mineral oil mixed with 0.5 (vol%) Span80 (Fluka Analytical), silicone oil (AR 20), silicone oil mixed with 0.2 (vol%) Triton X-100, fluorinated oil (HFE-7500 3MTM NovecTM) and olive oil (Bertolli). All materials were purchased from Sigma-Aldrich unless otherwise stated. The custom made platform was rotated by a PC fan (Coolink). Frequency of spinning was monitored by the tachometric output of the fan. We applied 360 rotations per minute (rpm) corresponding to a speed of 37 cm/s at the tip of the micropipette.

Once the dish was spinning, a glass micropipette (inner diameter $d = 50 \mu\text{m}$) was immersed into the oil from above to a depth of max 1 mm and a distance from the axis of rotation of 1 cm. The other end of the micropipette was connected to an elevated plastic syringe through a PTFE tube with an inner diameter of 1 mm, interrupted by a normally closed valve. The entire fluidic system was filled with deionized water (Seralpur AP30, Seral). After immersing the tip of the micropipette in the oil, the valve was opened for one minute. During this time, a flow commenced through the micropipette due to the applied hydrostatic pressure of 2500 Pa. As the water entered the rotating oil from the micropipette, it was separated into nanoliter scale droplets by the shear force acting on its surface. After one minute, the micropipette was removed, the rotation was stopped, and

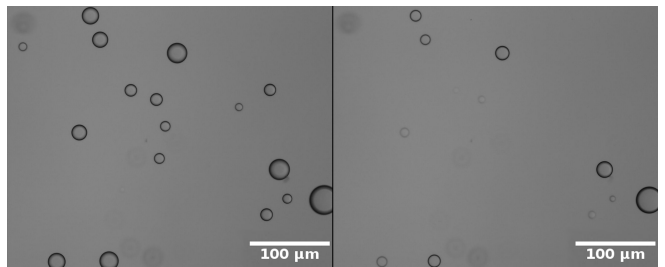


FIG. 1. Images of a field of view in two different time points observed on an inverted microscope, with 2.5 h in between. Water droplets were generated in silicone oil with no additives. Many small droplets ($d \approx 30 - 50 \mu\text{m}$) completely disappeared during this time, while the initially larger ones remained with a reduced diameter.

the Petri dish with the droplets inside was placed onto the microscope for time-lapse analysis.

B. Time-lapse analysis

Time-lapse recordings of the droplets were executed using an inverted microscope (Zeiss Axio Observer) equipped with a 10x EC Plan Neofluar objective, CMOS camera (Andor Zyla 5.5) and motorized stage (Marzhauser). The Petri dish with the w/o emulsion inside was placed onto the sample holder. Subsequently, fields of view (FoVs) with surface attached drops were identified and time-lapse imaging was programmed using the CellSorter software. Each FoV was recorded in brightfield mode every 5 minutes for a period of time that varied by experiment. For each FoV we used an auto-focusing algorithm to follow the equator of the droplets moving out of the focal plane as they shrank. A z-stack of three images was captured with a distance of $5 \mu\text{m}$ between the z-planes. Software chose the sharpest z-plane. The recorded images were stored for later analysis (see FIG. 1).

To determine the change of shape of the droplets in time from a side view, a custom developed contact angle measurement setup (Plosz Mernokiroda Ltd.) was used. A glass cuvette was filled with oil and a separated Petri dish bottom was placed into it. This was necessary in order to have the drops attach to the same surface as in the experiments with the inverted microscope described above. Water droplets were generated manually under the oil using a glass micropipette with an inner diameter of $50 \mu\text{m}$. Once a droplet with a size in the target range ($\approx 500 \mu\text{m}$) sedimented onto the surface, the magnifying optics was focused and the time-lapse imaging was started. Images were recorded every 15 minutes for a period of several days until the examined droplet completely disappeared.

C. Image analysis

Time-lapse images were analyzed with the ImageJ software [23]. Using an inverted microscope we could measure the diameter of the droplets with a shape of a spherical cap from a bottom view. Every field of view was treated as an image sequence in which the changing diameter of the droplets needs to be determined on each frame. First, the region of interest (RoI) in a given FoV was cut out (Fig. S6.1). Afterwards, a threshold was applied to each image using the Triangle algorithm [24], which separated the droplets from the background resulting in a binary image (Fig. S6.2). Subsequently, the built-in particle analyzer algorithm of ImageJ was applied on the binary image to identify the droplets (Fig. S6.3) and measure their diameter.

In case of the contact angle measurement, we used the DropSnake plugin [25] to analyze the side view images of the droplets (see Fig. S7). Contact angles were extracted every 2.5 hours. Around 8 points along the outline of the droplets were manually highlighted and then the edge was automatically fit by the algorithm. The contact diameter on the solid surface, the droplet diameter, and the left and right contact angles were calculated. The average of these two angles was accepted as the final contact angle value.

III. RESULTS

A. Time-lapse analysis of droplets

Generation of droplets was executed as described above, then the hydrophobic Petri dish containing the w/o emulsion of thousands of droplets was placed onto an inverted microscope. Time-lapse images were recorded to simultaneously observe multiple, similarly sized droplets under the same conditions. The change of the diameter of a number of such water droplets under mineral oil can be seen in Fig. 2a and Supplementary video 1. A perfect immiscibility between water and oil would dictate a constant size, however, time-lapse recordings show a gradual dissolution of the droplets. As indicated by a representative curve, the decrease in the diameter $d(t)$ of the droplets from a bottom view occurs in three distinct stages (labeled with numbers 1-3) beginning with a linear decrease, followed by a stagnating phase, and ending with a rapid decrease (Fig. 2b). In order to better understand this phenomenon, we executed another type of experiment: a water droplet placed under mineral oil was imaged from side view using a contact angle measurement setup. In both experiments the droplets were deposited on a hydrophobic plastic Petri dish surface, exhibiting an initial contact angle higher than 90° . The change of the contact angle and the contact diameter imaged from a side view can be seen in Fig. 3. It is apparent that the contact area between the droplet and the surface does not change in phases 1-2, but it quickly shrinks in

the final phase 3 of droplet dissolution.

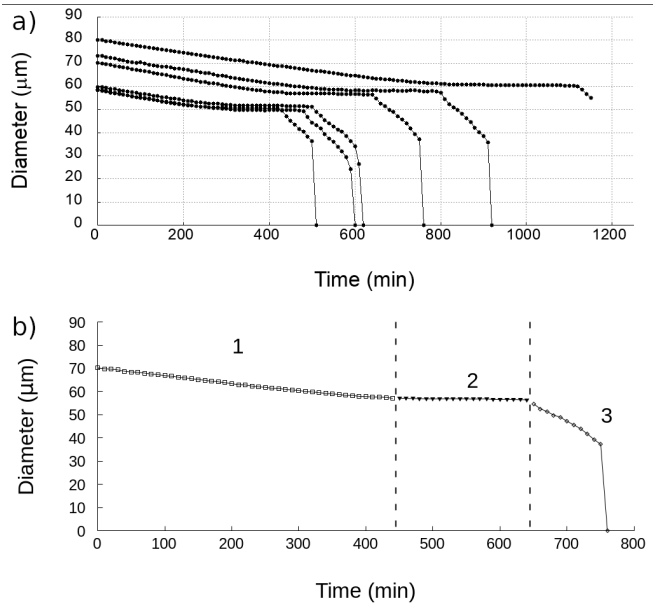


FIG. 2. a) Data showing the change of the diameter of water droplets under mineral oil from a bottom view as observed by the objective lens of an inverted microscope. Different curves correspond to different droplets. b) The three distinctive phases of a representative $d(t)$ curve.

According to these results a model can be proposed for the dissolution of the droplets and the change of their shape descriptors. During the entire process, the droplet shape can be described as a spherical cap sitting on a flat surface. In phase 1 the radius of the droplet decreases gradually due to the loss of droplet volume. In this phase the contact angle decreases, as well. Since the contact area does not change (Fig. 3.), this phase cor-

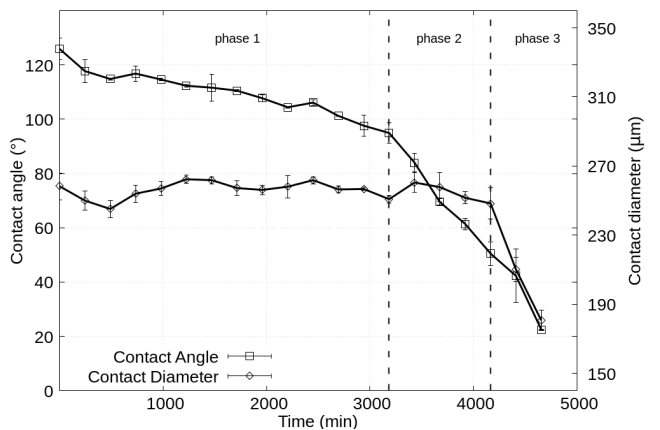


FIG. 3. The time evolution of shape descriptors of a droplet imaged from a side view. Vertical lines indicate the boundary between the three different phases. See also supplementary video 2.

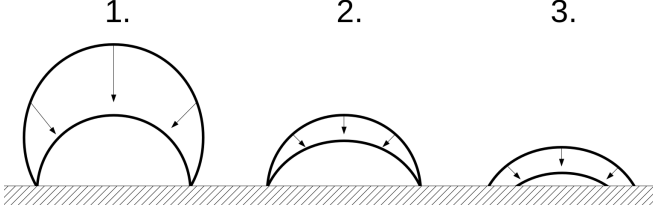


FIG. 4. 3 phase model of sessile droplet dissolution under a cover oil on a hydrophobic surface. Phase 1: The contact angle decreases together with the droplet diameter, while the contact area remains unchanged. Phase 2: After the contact angle reaches 90° , it keeps decreasing together with the volume of the droplet but with a constant diameter of its vertical projection being equal to the contact diameter. Phases 1 and 2 correspond to a pinning mode dissolution. Phase 3: The contact diameter and the contact angle decrease at the same time until complete disappearance of the droplet corresponding to a mixed mode dissolution.

responds to the pinning mode of evaporation (Fig. 4.1). Phase 2 begins when the contact angle reaches 90° . At this point the droplet is a hemisphere. Then the contact angle and volume of the droplet keep decreasing but with a constant diameter of its vertical projection being equal to the contact diameter (Fig. 4.2). In phase 3, the contact surface area rapidly shrinks together with the contact angle until complete dissolution. Thus this phase corresponds to a mixed mode (Fig. 4.3), whereas phases 1 and 2 correspond to the pinning mode of dissolution.

To investigate the generality of the phenomenon and identify any surfactant-induced effect, droplets under different oil mixtures were imaged in time-lapse mode on an inverted microscope. According to the empirical theory proposed by Picknett [13] and Erbil [17] for spherical droplets, the two third power of the volume of the droplets ($V^{2/3}$) should show a linear decrease in time. Thus, the square of the droplet diameter (d^2) is also expected to show a linear decrease in phase 1. This behaviour has indeed been reproduced by our time-lapse measurements for all four oil mixtures we studied in depth as Fig. 5 demonstrates. Droplets on a glass surface showed identical behaviour (Supplementary video 3). Water droplets in fluorinated oil or olive oil also gradually shrunk and disappeared on the timescale of hours (data not shown). In phase 1 both the volume and the contact angle of the droplets can be calculated from the measurements carried out on the inverted microscope (Fig. S2-4). However, the radius of the spherical cap in phase 2 and 3 cannot be easily measured using this setup. We could follow this radius until the end of the process using the contact angle measurement device. Interestingly, this quantity has a minimum when the shape of the droplet is a hemisphere (Fig. S5).

It is apparent, that the droplet size decreased significantly faster in silicone oil than in mineral oil. The pres-

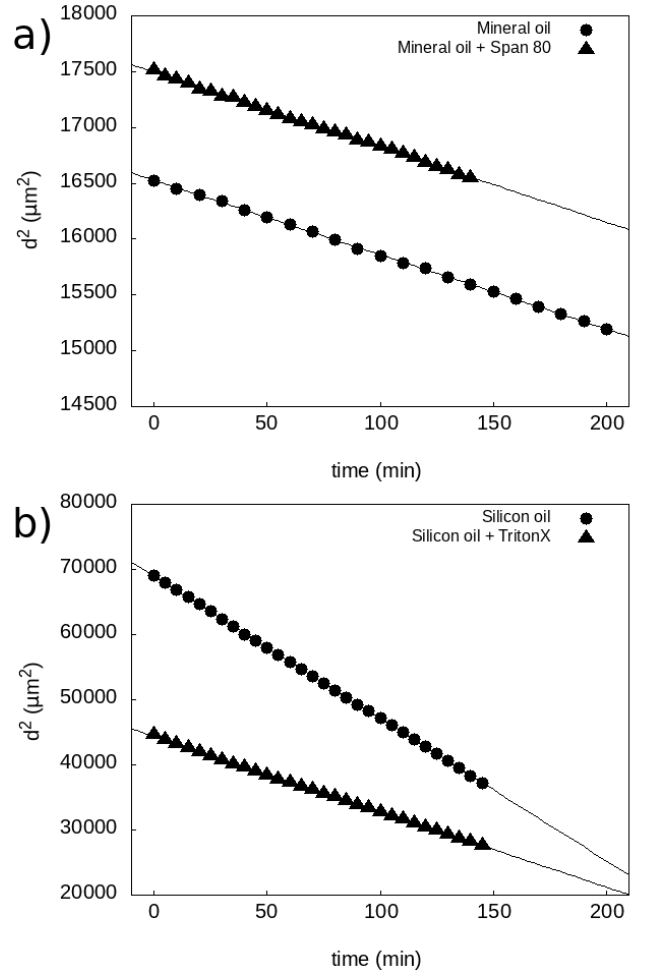


FIG. 5. Square of the droplet diameter $d^2(t)$ as a function of time in phase 1 measured on an inverted microscope. a) $d^2(t)$ curves for representative droplets in mineral oil and mineral oil mixed with surfactant (Span80). b) $d^2(t)$ curves for representative droplets in silicone oil and silicone oil mixed with surfactant (Triton X-100). Data series were fit with a line. Relative standard error of the slope was $< 1\%$ in all cases.

ence of surfactants in conventionally used concentrations did not impede dissolution.

We observed spontaneous microstructure formation on the surface of the water droplets in oils containing surfactant (Fig. S.8). During the dissolution process the droplet surface became cloudy and dark, exhibiting a rough morphology resembling the observations by Schmitt et al. [21].

B. Calculation of the diffusion coefficient and saturation density

The measurements presented here allow us to calculate some of the physical parameters characterizing the diffusion and solubility of water in oil. Water diffusion

can be described by the diffusion equation

$$\frac{\partial \rho(\mathbf{x}, t)}{\partial t} = D \Delta \rho(\mathbf{x}, t), \quad (1)$$

where $\rho(\mathbf{x}, t)$ denotes the mass density of water as a function of space (\mathbf{x}) and time (t); and D is its diffusion coefficient. Assuming stationarity (which is a good approximation if the oil-water interface moves much slower than the speed of the diffusion over the length-scale of the droplet) the diffusion equation simplifies to Laplace's equation:

$$\Delta \rho(\mathbf{x}) = 0. \quad (2)$$

For a spherical droplet or, equivalently, when a hemispherical droplet is sitting on the side of a half-space (as is the case at the end of phase 1 in our experiments) the most suitable choice for the coordinate system is the spherical one. Denoting the radial coordinate by r , Laplace's equation can be expressed as

$$\frac{1}{r^2} \partial_r (r^2 \partial_r \rho(r)) = 0. \quad (3)$$

Its solution that satisfies the boundary conditions $\rho(\infty) = 0$ and $\rho(R) = \rho_s$, where R is the radius of the droplet and ρ_s is the saturation density of water is

$$\rho(r) = \frac{R \rho_s}{r}. \quad (4)$$

The mass flux density from Fick's first law can be determined as

$$j(r) = -D \partial_r \rho(r) = \frac{D R \rho_s}{r^2}, \quad (5)$$

which, at the droplet boundary becomes

$$j(R) = \frac{D \rho_s}{R}. \quad (6)$$

This mass flux density can be directly determined from the time-lapse measurements. Close to the time point when the shape of the droplet is a hemisphere (which is equivalent to a sphere in the full space), the mass flux density is:

$$j(R) = -\rho_0 \frac{1}{A} \frac{dV}{dt} = -\frac{\rho_0}{2\pi R^2} \cdot 2\pi R^2 \frac{dR}{dt} = -\rho_0 \frac{dR}{dt} \quad (7)$$

where $\rho_0 \approx 10^3 \text{ kg/m}^3$ is the density of bulk water, and A and V denote the area and volume of the droplet of radius R , respectively. Plugging this expression into Eq. (6) results in

$$-2D \frac{\rho_s}{\rho_0} = \frac{2}{R} \frac{dR}{dt} = \frac{dR^2}{dt}, \quad (8)$$

which shows, in agreement with Fig. 5, that R^2 decreases linearly with time at a rate of

$$2D \frac{\rho_s}{\rho_0}. \quad (9)$$

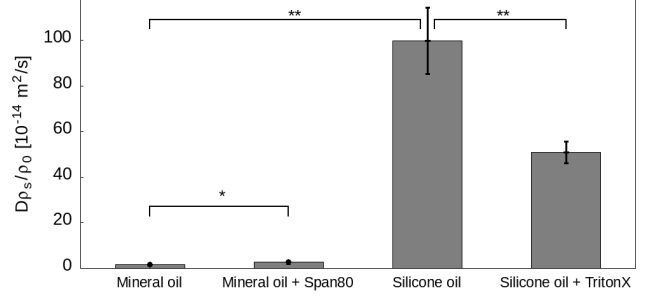


FIG. 6. Values of $D\rho_s/\rho_0$ of the four different oil mixtures we investigated in depth. For each material the data shown corresponds to a linear fit of five different droplets under the same conditions. Errors were calculated as the standard deviation of the five slopes. Significance levels: ** : $p < 0.01\%$, * : $p < 0.05\%$. Values of $D\rho_s/\rho_0$ are the following. Mineral oil: $(1.66 \pm 0.64) \times 10^{-14} \text{ m}^2/\text{s}$; mineral oil with 0.5 (vol%) Span80: $(2.78 \pm 0.70) \times 10^{-14} \text{ m}^2/\text{s}$; silicone oil: $(99.78 \pm 14.57) \times 10^{-14} \text{ m}^2/\text{s}$; silicone oil with 0.2 (vol%) Triton X-100: $(50.88 \pm 4.68) \times 10^{-14} \text{ m}^2/\text{s}$.

Measuring this rate provides the values of $D\rho_s/\rho_0$ for the four different cover oils investigated. This quantity characterizes the stability of the water droplets through two fundamental physical parameters: the diffusion coefficient and the saturation density of water in the specific oil. The results presented in Fig. 5 and summarized in Fig. 6 show that different oils can exhibit significantly different dissolution characteristics. Interestingly, the presence of a surfactant can change droplet stability in contrasting ways. In case of mineral oil, the rate of dissolution was increased by the presence of the surfactant Span80, while for silicon oil, it was decreased by a factor of 2 by the surfactant Tirtion X-100.

IV. DISCUSSION

Testing several chemically diverse oils including mineral, silicone, fluorinated, and olive oils we observed that nanoliter-sized water droplets dispersed in the oil gradually shrank and disappeared in a few hours. Application of surfactants did not have a qualitative impact on the phenomenon. We could readily monitor the volume and shape (contact angle) of water droplets under oil on a solid surface with time-lapse microscopy. Our experimental results fit well into the previously developed theoretical framework for the description of evaporating droplets under atmospheric conditions. We explain the observation by the dissolution and diffusion of water in oil, which allowed us to calculate the product of the diffusion coefficient and the relative saturation density of water in oil determining the rate of droplet dissolution. Data on the diffusion coefficient or saturation density of water in oils are sparse in the literature. Although vegetable oils can absorb $\sim 1000 \text{ ppm}$ water [26], saturation density in mineral oil at room temperature (25°C) was

reported to be only ~ 70 ppm [27]. Diffusion coefficient of water in paraffin oil and in groundnut oil was found to be $8.5 \times 10^{-10} \text{ m}^2/\text{s}$ and $2.5 \times 10^{-10} \text{ m}^2/\text{s}$ at room temperature, respectively [28]. Considering mineral oil as a reference, our results lie in the expected range. Our method offers a simple way to measure the diffusion coefficient or saturation density of immiscible liquids using only a small volume, when one of these quantities is already known.

We believe that our findings have significant implications for the design of devices using sparse emulsions in droplet microfluidics and nanoliter- or picoliter-scale droplet printing under oil. When the concentration of reagents in the nanoliter- or picoliter-sized aqueous

droplets is critical, we suggest to consider and calibrate for droplet dissolution, especially in long term applications. Moreover, we believe that the discovered phenomenon can be exploited to initiate well controlled, concentration dependent reactions in tiny volumes.

ACKNOWLEDGMENTS

This work was supported by the Hungarian National Research, Development and Innovation Office (grant numbers: PD 124559 for R. U. S., KH-17, KKP 129936 and ERC-HU for R. H.), and the Lendület Program of the Hungarian Academy of Sciences for R. H.

-
- [1] A. D. Griffiths and D. S. Tawfik, Miniaturising the laboratory in emulsion droplets, *Trends in biotechnology* **24**, 395 (2006).
 - [2] T. F. Tadros, Fundamental principles of emulsion rheology and their applications, *Colloids and Surfaces A: Physicochemical and Engineering Aspects* **91**, 39 (1994).
 - [3] D. A. Weitz, Perspective on droplet-based single-cell sequencing, *Lab on a Chip* **17**, 2539 (2017).
 - [4] Y. Ding, J. Choo, and A. J. Demello, From single-molecule detection to next-generation sequencing: microfluidic droplets for high-throughput nucleic acid analysis, *Microfluidics and Nanofluidics* **21**, 58 (2017).
 - [5] N. Shembekar, C. Chaipan, R. Utharala, and C. A. Merten, Droplet-based microfluidics in drug discovery, transcriptomics and high-throughput molecular genetics, *Lab on a Chip* **16**, 1314 (2016).
 - [6] S. Haeberle and R. Zengerle, Microfluidic platforms for lab-on-a-chip applications, *Lab on a Chip* **7**, 1094 (2007).
 - [7] B. Francz, R. Ungai-Salánki, É. Sautner, R. Horvath, and B. Szabó, Subnanoliter precision piezo pipette for single-cell isolation and droplet printing, *Microfluidics and Nanofluidics* **24**, 12 (2020).
 - [8] L. Rosenfeld, T. Lin, R. Derda, and S. K. Tang, Review and analysis of performance metrics of droplet microfluidics systems, *Microfluidics and nanofluidics* **16**, 921 (2014).
 - [9] L. Mazutis, J. Gilbert, W. L. Ung, D. A. Weitz, A. D. Griffiths, and J. A. Heyman, Single-cell analysis and sorting using droplet-based microfluidics, *Nature protocols* **8**, 870 (2013).
 - [10] R. K. Shah, H. C. Shum, A. C. Rowat, D. Lee, J. J. Agresti, A. S. Utada, L.-Y. Chu, J.-W. Kim, A. Fernandez-Nieves, C. J. Martinez, *et al.*, Designer emulsions using microfluidics, *Materials Today* **11**, 18 (2008).
 - [11] J.-C. Baret, Surfactants in droplet-based microfluidics, *Lab on a Chip* **12**, 422 (2012).
 - [12] Y. Zhu, Y.-X. Zhang, W.-W. Liu, Y. Ma, Q. Fang, and B. Yao, Printing 2-dimensional droplet array for single-cell reverse transcription quantitative pcr assay with a microfluidic robot, *Scientific reports* **5**, 9551 (2015).
 - [13] R. Picknett and R. Bexon, The evaporation of sessile or pendant drops in still air, *Journal of Colloid and Interface Science* **61**, 336 (1977).
 - [14] D. M. Soolaman and H.-Z. Yu, Water microdroplets on molecularly tailored surfaces: correlation between wetting hysteresis and evaporation mode switching, *The Journal of Physical Chemistry B* **109**, 17967 (2005).
 - [15] M. Lurie and N. Michailoff, Evaporation from free water surface, *Industrial & Engineering Chemistry* **28**, 345 (1936).
 - [16] H. Y. Erbil, G. McHale, S. M. Rowan, and M. Newton, Analysis of evaporating droplets using ellipsoidal cap geometry, *Journal of adhesion science and technology* **13**, 1375 (1999).
 - [17] H. Y. Erbil, G. McHale, and M. Newton, Drop evaporation on solid surfaces: constant contact angle mode, *Langmuir* **18**, 2636 (2002).
 - [18] P. S. Epstein and M. S. Plesset, On the stability of gas bubbles in liquid-gas solutions, *The Journal of Chemical Physics* **18**, 1505 (1950).
 - [19] J. T. Su and D. Needham, Mass transfer in the dissolution of a multicomponent liquid droplet in an immiscible liquid environment, *Langmuir* **29**, 13339 (2013).
 - [20] P. B. Duncan and D. Needham, Microdroplet dissolution into a second-phase solvent using a micropipet technique: Test of the epstein- plesset model for an aniline- water system, *Langmuir* **22**, 4190 (2006).
 - [21] M. Schmitt, R. Toor, R. Denoyel, and M. Antoni, Spontaneous microstructure formation at water/paraffin oil interfaces, *Langmuir* **33**, 14011 (2017).
 - [22] P. Umbanhowar, V. Prasad, and D. A. Weitz, Monodisperse emulsion generation via drop break off in a coflowing stream, *Langmuir* **16**, 347 (2000).
 - [23] J. Schindelin, I. Arganda-Carreras, E. Frise, V. Kaynig, M. Longair, T. Pietzsch, S. Preibisch, C. Rueden, S. Saalfeld, B. Schmid, *et al.*, Fiji: an open-source platform for biological-image analysis, *Nature methods* **9**, 676 (2012).
 - [24] G. W. Zack, W. E. Rogers, and S. Latt, Automatic measurement of sister chromatid exchange frequency., *Journal of Histochemistry & Cytochemistry* **25**, 741 (1977).
 - [25] A. F. Stalder, G. Kulik, D. Sage, L. Barbieri, and P. Hoffmann, A snake-based approach to accurate determination of both contact points and contact angles, *Colloids and surfaces A: physicochemical and engineering aspects* **286**, 92 (2006).
 - [26] M. Hilder, The solubility of water in edible oils and fats,

- Journal of the American Oil Chemists Society **45**, 703 (1968).
- [27] Y. Du, A. V. Mamishev, B. C. Lesieutre, M. Zahn, and S.-H. Kang, Moisture solubility for differently conditioned transformer oils, IEEE transactions on Dielectrics and Electrical Insulation **8**, 805 (2001).
- [28] M. Hilderand M. van den Tempe, Diffusivity of water in groundnut oil and paraffi oil, Journal of Applied Chemistry and Biotechnology **21**, 176 (1971).

Supplementary material to: Long-term instability of water in oil microdroplets

Tams Gerecsei, Rita Ungai-Salanki, Andras Saftics,
Imre Deryi, Robert Horvath, Balint Szabo

March 22, 2022

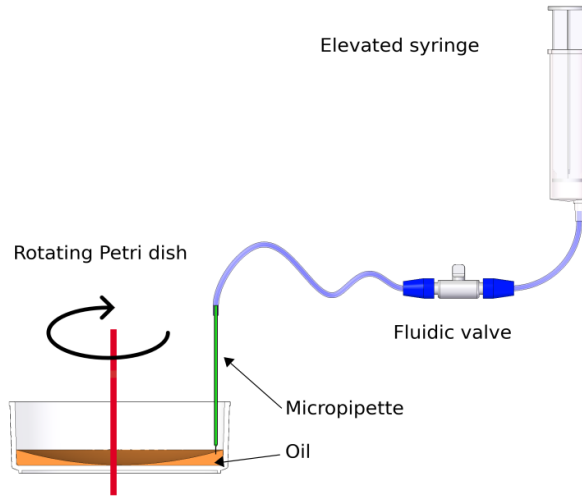


Figure 1: Schematic demonstration of our droplet generation method. The tubing is filled with deionized water and connected to the vertical micropipette immersed into the spinning Petri dish with the oil inside.

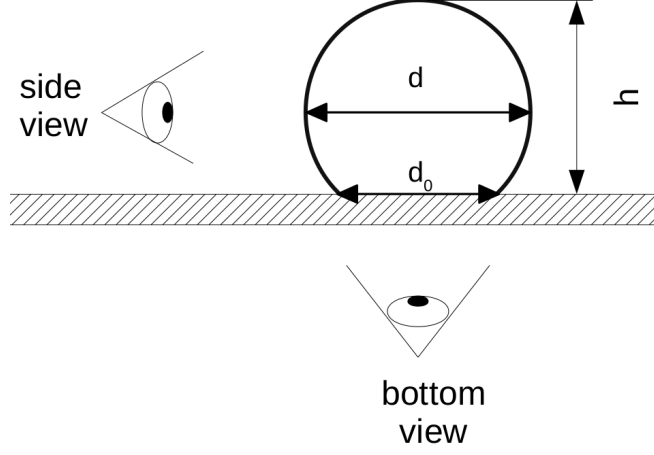


Figure 2: Geometry of a sessile droplet on a hydrophobic surface. d is the diameter of the spherical droplet at its equator, while d_0 is the contact diameter.

Calculation of the droplet volume from the time-lapse images The geometry of a sessile droplet can be described by a spherical cap. On a hydrophobic surface the contact angle is larger than 90° in equilibrium. Thus the equator of the droplet with a diameter of d is above the solid surface. This was the case in the first phase of dissolution in our experiments. The diameter of the contact area with the solid surface is d_0 . These two parameters determine the overall volume of the droplet:

$$V_{droplet} = \frac{1}{6} \pi h \left[3 \left(\frac{d_0}{2} \right)^2 + h^2 \right] \quad (1)$$

where the height of the droplet:

$$h = \frac{d}{2} + \sqrt{\left(\frac{d}{2} \right)^2 - \left(\frac{d_0}{2} \right)^2} \quad (2)$$

As long as $d > d_0$, i.e., in phase 1 of the droplet dissolution (Fig.4.1.), d can be determined on an inverted microscope by observing the droplet from a bottom view. d_0 can be measured as the constant diameter of the droplet from a bottom view during the second phase of dissolution (Fig.4.2.). The contact angle (θ) of the droplet can also be calculated from these two diameters:

$$\theta = 180^\circ - \arcsin \left(\frac{d_0}{d} \right). \quad (3)$$

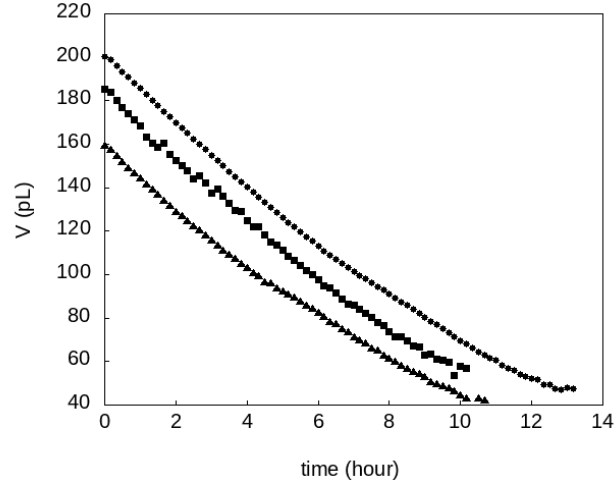


Figure 3: Volume of three representative droplets under mineral oil in phase 1 as measured on an inverted microscope, and calculated from eq.1.

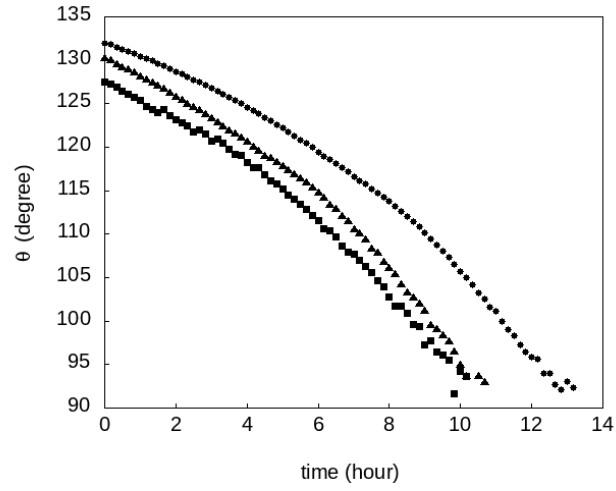


Figure 4: Contact angle of the droplets shown in Fig.S.3. calculated from eq.3.

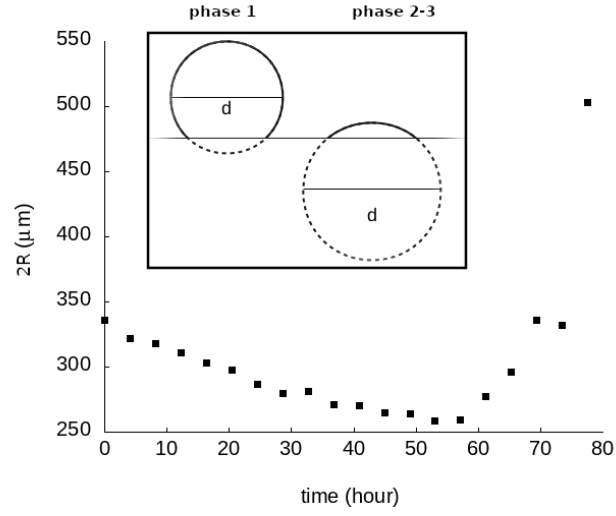


Figure 5: Droplet's radius of curvature determined on the basis of side view imaging. As it can be seen in the box, in phase 1 the radius decreases until the shape of the droplet reaches a hemisphere. After this minimum, the radius of curvature starts to increase in phases 2 and 3.

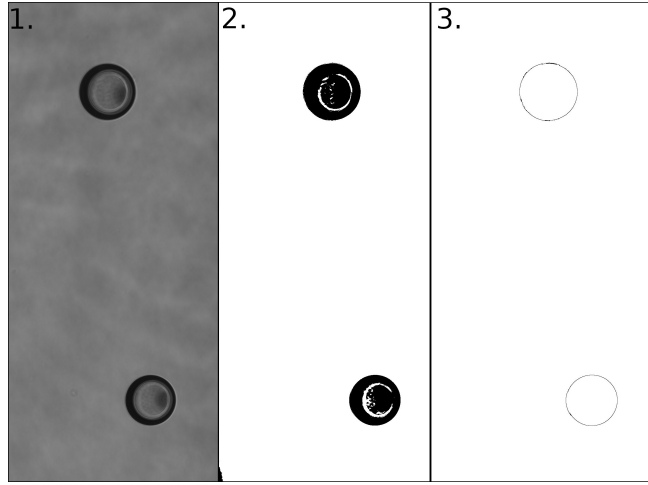


Figure 6: Three steps of image analysis applied on the time-lapse image sequences recorded on an inverted microscope. 1: The region of interest was cut out from the field of view. 2: Threshold was applied to separate the droplets from the background. 3.: Particle Analysis algorithm was utilized to identify and measure the diameter of droplets.

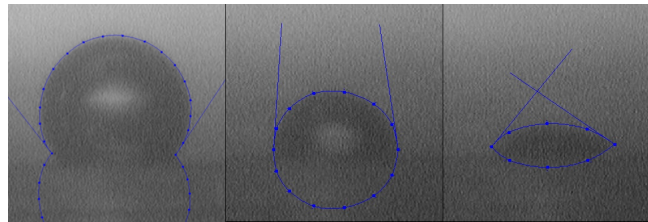


Figure 7: Evaluation of contact angle measurements in three different images. The blue points correspond to manually placed markers which were then used by the DropSnake plugin of ImageJ to fit a spherical cap on the droplets. The shape descriptors were automatically calculated and saved.

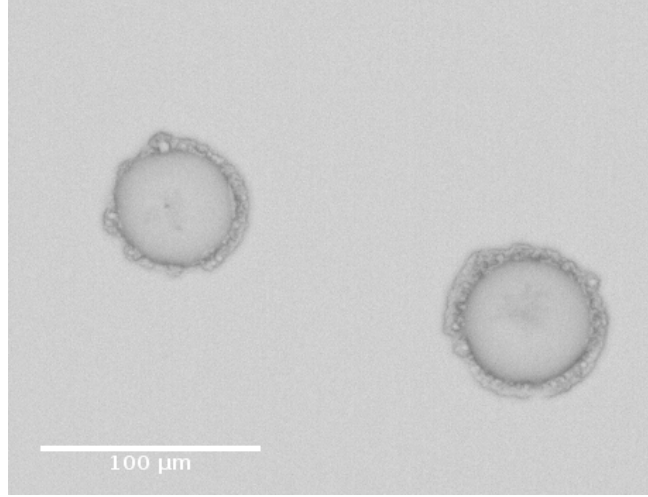


Figure 8: Water droplets in mineral oil supplemented with the surfactant Span80. After 2 hours the edge of the droplets started to exhibit a foam-like morphology, likely due to spontaneous microstructure formation.

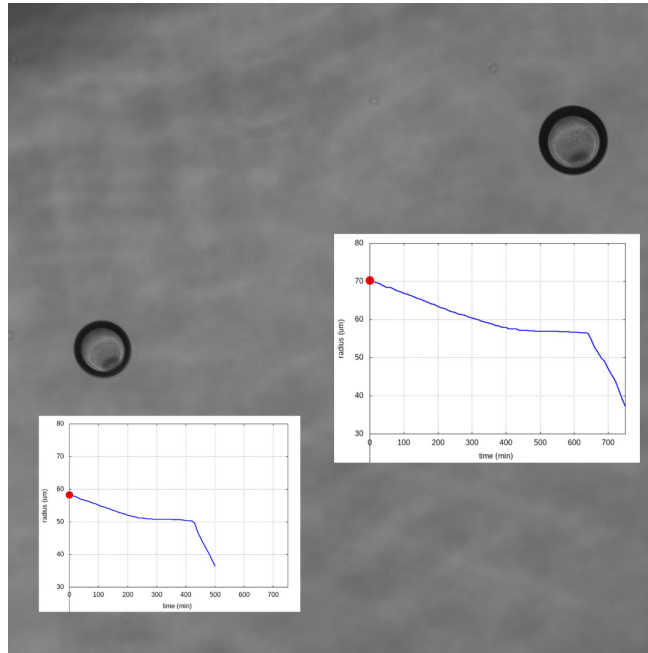


Figure 9: Supplementary video 1: Time-lapse video showing the dissolution of two sessile droplets under mineral oil on a hydrophobic Petri dish surface imaged on an inverted microscope. The curves show the evolution of the radius of the corresponding droplets. From this bottom view the vertical projection of the droplet can be observed. The three phases of dissolution discussed in the paper can be well distinguished on the curves as well as on the images.

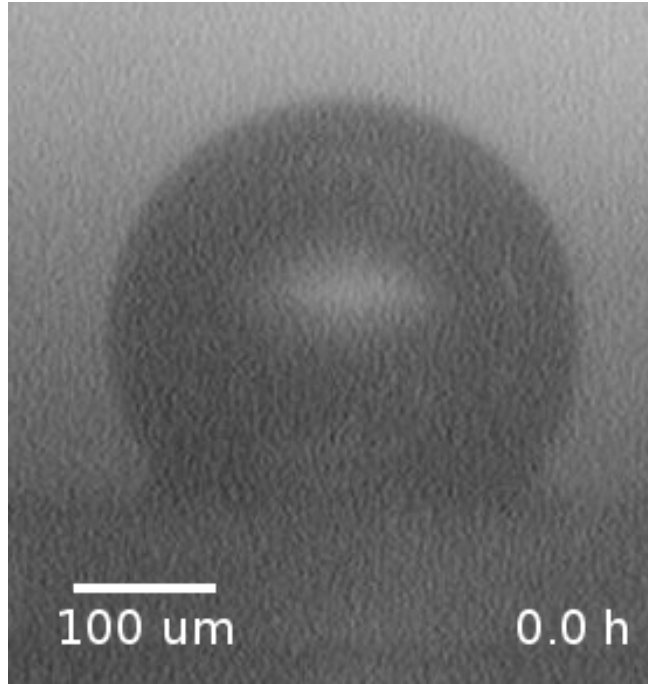


Figure 10: Supplementary video 2: Dissolution of a sessile water droplet under mineral oil sitting on a hydrophobic plastic surface observed from a side view. Values of diameter and contact angle as a function of time are shown in Fig.3. in the main text. The droplet exhibits a spherical cap shape during the process, which takes 11.5 days to complete.

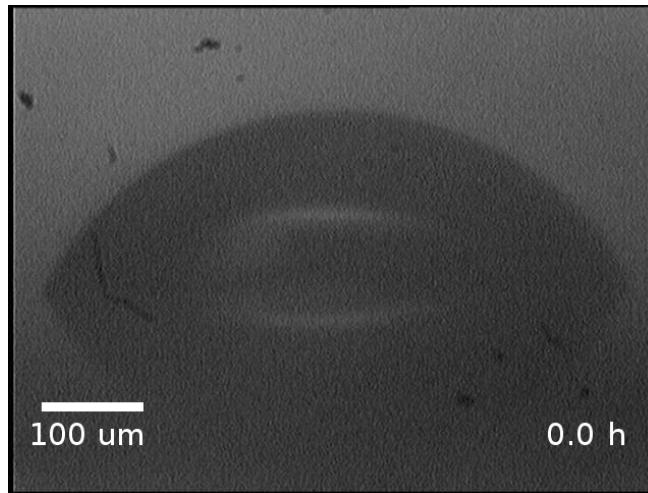


Figure 11: Supplementary video 3: Dissolution of a sessile water droplet under mineral oil sitting on a hydrophilic glass surface observed from a side view. The complete dissolution of the droplet happens in a pinning mode, whereby the contact angle change compensates for volume loss while the contact area remains constant.